Dalton Transactions

An international journal of inorganic chemistry

Accepted Manuscript

This article can be cited before page numbers have been issued, to do this please use: J. Beyer, M. Böhme, M. Rams, C. Nather and W. Plass, *Dalton Trans.*, 2026, DOI: 10.1039/D6DT00621C.

ROYAL SOCIETY OF CHEMISTRY

rsc.li/dalton

View Article Online
DOI: 10.1039/D6DT00621C

ARTICLE

Disentangling anisotropy and exchange in $Co(NCX)_2$ (X = S, Se) chains via THz-EPR spectroscopy

Received 00th January 20xx,
Accepted 00th January 20xx

DOI: 10.1039/x0xx00000x

Jooris Beyer[a], Michael Böhme[a], Michał Rams[b]*, Christian Näther[c]* and Winfried Plass[a]*

Two isostructural cobalt(II) chain compounds, $[Co(NCX)_2(py)_2]_n$ (X = S, Se) based on μ-1,3-bridging selenocyanate (**1**) and thiocyanate (**2**) ligands, were investigated to elucidate the effect of chalcogen substitution on magnetic anisotropy and exchange interactions. Both compounds form linear chains of octahedrally coordinated cobalt(II) ions with identical topology and similar magnetic exchange but different anisotropy. Heat capacity measurements reveal slightly stronger intrachain interactions and higher ordering temperatures for the selenocyanate derivative, while demonstrating a pronounced sensitivity of the critical temperature to sample handling. Frequency-domain Fourier-transform THz-EPR spectroscopy provides direct access to low-energy magnetic excitations, allowing the determination of intrachain excitation energies and effective g_z values without reliance on a specific model. The selenocyanate compound exhibits both a larger chain excitation gap and enhanced axial anisotropy. Temperature-dependent THz-EPR further yields estimates of weak interchain coupling that is essential for long-range magnetic ordering. Ab initio CASSCF/CASPT2/RASSI-SO calculations reproduce the experimental trends and reveal that the enhanced anisotropy in **1** originates primarily from the softer donor character of selenium, leading to increased covalency and enhanced spin–orbit coupling at the cobalt center, while axial ligand orientation dominates the single-ion anisotropy. Together, these results demonstrate how subtle ligand substitution modulates anisotropy and exchange in ferromagnetic cobalt(II)-based Ising chains.

Introduction

Low-dimensional magnetic materials have attracted sustained interest as model systems to investigate the interplay between single-ion anisotropy and magnetic exchange interactions.[1] In particular, cobalt(II)-based one-dimensional coordination polymers exhibit a rich magnetic behavior ranging from single-chain magnet (SCM) behavior to long-range magnetic ordering.[2] In such systems, the magnetic response is governed by the balance between strong axial single-ion anisotropy and intrachain exchange coupling, which together define the effective energy scale for spin reversal.[3,4] While slow relaxation in SCMs requires interchain interactions to remain sufficiently weak,[5,6,7] finite coupling in real materials often induces three-dimensional long-range magnetic ordering at low temperatures.[8,9–11] In some cases, SCM behavior can even coexist with antiferromagnetic correlations, reflecting a delicate balance of competing interactions.[12] These compounds are therefore more appropriately described as Ising-type cobalt(II) chain systems with magnetic ordering, providing experimentally accessible platforms to probe the microscopic origin of magnetic energy barriers.

Cobalt(II) thiocyanate coordination polymers of the general composition $[Co(NCS)_2(L)_2]_n$ represent a well-established family of octahedrally coordinated chain compounds in which the magnetic easy axis is oriented approximately along the L–Co–L direction, consistent with strong axial anisotropy.[6,11,13,14] Extensive studies have demonstrated that variation of the neutral coligand (L) only weakly affects the intrachain interaction, in line with the negligible participation of the coligand in the magnetic superexchange pathway.[6,10,11] To more directly influence both exchange and anisotropy, substitution of the anionic ligand by its heavier analogue has been explored. Replacement of thiocyanate by selenocyanate in $[Co(NCS)_2(pyridine)_2]_n$ affords an isotypic compound,[15] and mixed crystals $[Co(NCS)_{2-x}(NCSe)_x(pyridine)_2]_n$ exhibit a pronounced increase in the effective intrachain exchange constant J_{Ising} with increasing selenium content.[16] While these studies established a clear influence of chalcogen substitution on magnetic energy scales, the microscopic origin of this effect has remained unresolved.

In particular, it has not been clarified whether the enhanced magnetic barrier in the selenocyanate analogue originates predominantly from modified intrachain exchange coupling or from changes in single-ion anisotropy. Because heavier chalcogen donors are expected to enhance covalency and ligand-induced spin–orbit coupling contributions at the cobalt center,[17] a systematic investigation of the anisotropy is essential for a mechanistic understanding. Experimental and theoretical approaches to quantify single-ion anisotropy in Co(II) systems include THz spectroscopy and multireference ab initio methods.[18] However, reliable assessment of single-ion anisotropy requires high-quality crystallographic data suitable for multireference ab initio calculations. While such data

[a] Institut für Anorganische und Analytische Chemie, Friedrich-Schiller-Universität Jena, Humboldtstr. 8, 07743 Jena, Germany.
[b] Institute of Physics, Jagiellonian University, Łojasiewicza 11, 30348 Kraków, Poland.
[c] Institut für Anorganische Chemie, Christian-Albrechts-Universität zu Kiel, Max-Eyth-Straße 2, 24118 Kiel, Germany.
† Footnotes relating to the title and/or authors should appear here.

View Article Online
DOI: 10.1039/D6DT00631G

were available for the thiocyanate compound, the selenocyanate analogue was previously accessible only as microcrystalline material, and structural disorder in earlier crystallographic models of the sulfur compound further complicated a consistent comparison.[5,15,16]

Beyond these structural limitations, conventional thermodynamic measurements primarily probe collective magnetic behavior and do not directly disentangle contributions arising from single-ion anisotropy, intrachain exchange, and weak interchain coupling. Spectroscopic access to intrachain excitation energies and to the onset of magnetic ordering has so far remained largely unexplored in this class of cobalt(II) chain compounds.

Herein, we overcome these limitations and present a comprehensive comparative study of the isostructural cobalt(II) chain compounds $[Co(NCX)_2(pyridine)_2]_n$ (X = Se, S) based on phase-pure samples and disorder-free low-temperature crystal structures, enabling for the first time a direct and structurally consistent comparison of the sulfur and selenium analogues. By combining heat capacity measurements, frequency-domain Fourier-transform (FD-FT) THz-EPR spectroscopy, and CASSCF/CASPT2/RASSI-SO calculations, we demonstrate that single-ion anisotropy, intrachain exchange interactions, and interchain coupling can be disentangled within a unified framework. THz-EPR spectroscopy provides direct access to low-energy intrachain excitations and allows spectroscopic detection of the onset of three-dimensional magnetic ordering, yielding an independent determination of the ordering temperature.

Our results demonstrate that chalcogen substitution primarily enhances the single-ion anisotropy, whereas the intrachain exchange coupling is only weakly affected. The quantitative analysis based on the Lines model indicates only minor changes in the exchange interaction upon substitution. In contrast, the enhanced anisotropy dominates the intrachain excitation energy scale. The differences in the magnetic ordering temperatures, however, are primarily governed by interchain interactions, which are influenced by subtle structural changes such as reduced interchain separations in the selenocyanate compound. This finding clarifies the microscopic origin of the modified magnetic energy scale in the selenocyanate analogue and establishes these structurally well-defined cobalt(II) chains as a model system for systematically disentangling anisotropy and exchange in anisotropic one-dimensional magnets.

Experimental section

General and instrumentation

$Co(NO_3)_2{\cdot}6H_2O$ (99%) and $Co(NCS)_2$ (99.9%) were purchased from Sigma-Aldrich, whereas KSeCN (98.5%) and pyridine were obtained from Alfa Aesar and were all used without further purification. The precursor complex $[Co(NCSe)_2(py)_4]$ was synthesized according to the literature procedure.[15] Both chain compounds have been reported previously.[5,15] In the present work they were resynthesized to obtain phase-pure samples suitable for THz-EPR and heat capacity measurements. All reaction products were characterized by IR spectroscopy and powder X-ray diffraction (PXRD). For compound **2**, an elemental analysis was performed to confirm bulk purity. Elemental analyses were carried out using a vario MICRO cube instrument (Elementar Analysensysteme GmbH). However, this was not possible for the selenium-containing compound **1**, as the formation of solid SeO_2 during combustion is incompatible with the separation columns of the CHN analyzer. For compound **1**, phase purity was instead confirmed by comparing the experimental PXRD pattern with the pattern simulated from the single-crystal X-ray data (see Fig. S4). IR spectra were recorded at room temperature on a Bruker Vertex70 FT-IR spectrometer equipped with a broadband spectral range extension (VERTEX FM) covering the mid and far IR regions.

Synthesis of $[Co(NCSe)_2(py)_2]_n$ (1)

$Co(NO_3)_2{\cdot}6H_2O$ (145.5 mg, 0.5 mmol) and KSeCN (144.1 mg, 1 mmol) were stirred in ethanol (10 mL) for 2 h. The resulting precipitate was filtered off, and pyridine (20 µL, 0.25 mmol) was added to the filtrate. The solvent was allowed to evaporate very slowly, yielding small red crystals of **1** suitable for single-crystal X-ray diffraction. PXRD measurements revealed that phase-pure bulk material could not be obtained by this route, as trace amounts of the pyridine-rich complex $[Co(NCSe)_2(py)_4]$ were consistently present. Therefore, larger quantities of phase-pure **1** were prepared by thermal annealing of $[Co(NCSe)_2(py)_4]$ at 110 °C for 2 h, following the procedure described in the literature.[15] This procedure reproducibly afforded pure **1**, as confirmed by PXRD.

Synthesis of $[Co(NCS)_2(py)_2]_n$ (2)

Compound **2** was prepared following the procedure reported in the literature with slight modifications.[5] $Co(NCS)_2$ (522 mg, 3 mmol) and pyridine (8.0 µL, 1 mmol) were stirred in water (3 mL) at room temperature for 2 d. The resulting precipitate was collected by filtration, washed with only small amounts of ethanol and diethyl ether, and dried under vacuum. Single crystals suitable for X-ray diffraction were obtained by slow evaporation of the solvent from the filtrate. Elemental analysis: calc. (%) for $C_{12}H_{10}CoN_4S_2$: C, 43.2; H, 3.0; N, 16.8; S, 19.2; found: C, 43.05; H, 2.9; N, 16.7; S, 19.3.

Single-crystal structure analyses

Single-crystal X-ray diffraction data were collected on a Rigaku Synergy diffractometer equipped with a microfocus X-ray tube using Cu Kα radiation (λ = 1.54184 Å). Structure solutions were performed with SHELXT,[19] and refinements were performed against F^2 using SHELXL-2016.[20] All non-hydrogen atoms were refined with anisotropic displacement parameters. Hydrogen atoms were placed in calculated positions and refined using a riding model with $U_{iso}(H)$ = 1.2 $U_{eq}(C)$. Selected crystallographic data and refinement details are provided in Table S1. CCDC-2523198 (**1**) and CCDC-2523199 (**2**) contain the supplementary crystallographic data for the structures in this paper.

Powder X-ray diffraction

Powder X-ray diffraction (PXRD) measurements were performed on a STOE STADI P transmission diffractometer equipped with Cu $K\alpha_1$ radiation source (λ = 1.540598 Å), a Ge(111) monochromator (STOE & Cie), and a MYTHEN 1K detector (Dectris).

Heat capacity measurements

Heat capacity measurements were carried out using the relaxation technique as implemented in a Quantum Design Physical Property Measurement System (PPMS). Apiezon N grease was used to ensure good thermal contact between the sample and the sample holder.

View Article Online
DOI: 10.1039/D6DT00621C

The addenda were measured prior to each experiment and subtracted from the total signal. Unless stated otherwise, measurements were performed on non-pressed powder samples.

Magnetic susceptibility measurements

Magnetic susceptibility measurements were performed using a Quantum Design MPMS XL SQUID magnetometer under an applied dc field of 100 Oe. Powder samples were immobilized in Nujol inside gelatin capsules and cooled to low temperature in zero field to prevent grain reorientation under the applied magnetic field.

FD-FT THz-EPR Spectroscopy

Low-temperature FD-FT THz-EPR measurements were carried out at the THz-EPR beamline of the BESSY II synchrotron facility at Helmholtz-Zentrum Berlin (HZB). The experimental setup has been described in detail elsewhere.[21] In brief, the spectrometer consists of a high-resolution FT-IR spectrometer equipped with a Hg arc lamp for high-energy regions and coupled to a synchrotron source operating in low-α mode for the low-energy region, an evacuated quasi-optical transmission line, a 12 T superconducting magnet, and a Si bolometer detector. Polycrystalline samples were homogenized with polyethylene (PE) in a mortar and pressed into pellets. Spectra were recorded in Voigt geometry with a spectral resolution of 1 cm^{-1} (Hg arc lamp) and 0.5 cm^{-1} (low-α radiation) over a magnetic field range of 0–10 T. For the latter, a resolution of 0.5 cm^{-1} with a digital data spacing of 0.015 cm^{-1} was used. Based on the standard deviation of peak positions (< 0.04 cm^{-1}) and the high signal-to-noise ratio (384 scans), the experimental precision is estimated to be 0.02–0.03 cm^{-1}, justifying the significance of the discussed peak shifts. Data processing was performed using MATLAB (version R2022a).[17] Magnetic-field division spectra (MDS) were obtained by dividing each spectrum by a spectrum recorded at a magnetic field lower by 1 T. Magnetic-field subtraction spectra (MSS) were generated by subtracting the zero-field spectrum from spectra recorded under applied magnetic fields.

Computational Details

Ab initio calculations were performed on structural models representing the two crystallographically independent cobalt(II) centers in compounds **1** and **2**, namely $[CoZn_2(NCSe)_4(py)_2]^{2+}$ (denoted as **1**-Co1 and **1**-Co2) and $[CoZn_2(NCS)_4(py)_2]^{2+}$ (denoted as **2**-Co1 and **2**-Co2), respectively, derived from the experimentally determined single-crystal structures (Fig. S1). Two terminal zinc(II) ions were introduced to compensate the negative molecular charge. Hydrogen atom positions were optimized at the RI-DFT[22]/BP86[23]/def2-SVP[24] level of theory using the Turbomole 7.6 program package.[25] To facilitate SCF convergence during geometry optimizations, the paramagnetic cobalt(II) ions were replaced by diamagnetic zinc(II) ions. Single-ion electronic structure data were subsequently obtained from CASSCF/CASPT2/RASSI-SO calculations and employed in the POLY_ANISO program[26] to model the magnetic properties within an *n*-membered spin-ring approach.[4] The intrachain exchange coupling constant J_{Lines} was determined following the procedure established in the literature.[4] Simulations with different *n*-membered spin ring sizes enabled extrapolation of the magnetic susceptibility of **1** and **2** to the infinite-chain limit ($n \rightarrow \infty$) in the temperature range of 4–50 K. Weak interchain interactions were incorporated via a mean-field approach, where *zJ'* represents the effective interchain coupling.[4]

Results and discussion

Synthesis and crystal structures

Single crystals of the selenium compound **1** were obtained from the reaction of cobalt(II) nitrate hexahydrate with potassium selenocyanate in ethanol. For the sulfur analogue **2**, single crystals were also prepared and the structure was redetermined at 100 K for direct comparison with **1** (see Experimental Section), as the previously reported structure exhibits pyridine disorder. Powder X-ray diffraction (PXRD) investigations (Fig. S2) and IR spectroscopy (Fig. S3) confirm that phase-pure samples of **2** were obtained, consistent with the literature data.[5]

In contrast, initial batches of the selenium compound **1** were contaminated with varying amounts of the pyridine-rich mononuclear species $[Co(NCSe)_2(pyridine)_2]$. Therefore, this precursor was first prepared as a pure material (Figs. S4 and S5) and subsequently thermally annealed following the literature procedure.[15] PXRD confirms that compound **1** was thereby obtained as a pure crystalline phase, exhibiting an IR spectrum identical to that reported previously (Figs. S6 and S7).[15,16]

Whereas the structure of the sulfur analogue **2** has already been reported in the literature,[5] the present single-crystal data allow a direct comparison with the selenium derivative **1**. Since compounds **1** and **2** are isotypic, only the key structural features relevant to magnetic exchange and anisotropy are discussed below.

Compounds **1** and **2** crystallize in the centrosymmetric space group $P\bar{1}$ (No. 2) with $Z = 3$ formula units per unit cell (Table S1). The asymmetric unit contains two crystallographically independent cobalt cations, one (Co1) in a general position and one (Co2) on an inversion center, together with three crystallographically independent pyridine molecules and three independent anionic ligands, all occupying general positions (Fig. S8).

In both compounds, the cobalt(II) ions are octahedrally coordinated by two *trans*-N- and two *trans*-S- (**2**) or *trans*-Se-bonding (**1**) thiocyanate/selenocyanate anions and two *trans* pyridine coligands occupying the axial positions. The Co–N and Co–S/Co–Se bond lengths of the crystallographically independent cobalt centers are comparable, and the bond angles indicate slightly distorted octahedral coordination environments (Table S2). Continuous shape measures (CShM, Table S3) reveal somewhat

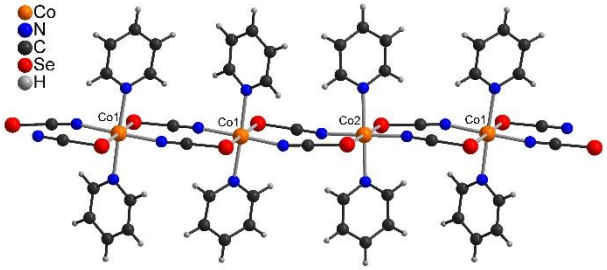

Fig. 1 Repeating unit of the linear chains in the crystal structure of compound **1**, illustrating the [Co1···Co1···Co2] sequence. ORTEP representations of compounds **1** and **2** are shown in Fig. S8.

larger distortions for compound **1** ($S(O_h)$ = 1.611/1.711 for Co1/Co2) compared to compound **2** ($S(O_h)$ = 1.141/1.193), indicating a slightly enhanced deviation from ideal octahedral symmetry in the selenium derivative. An overlay of the coordination environments of Co1 and Co2 is shown in Fig. S9.

The octahedrally coordinated cobalt centers are linked by centrosymmetric pairs of μ-1,3-bridging anions (**1**: selenocyanate; **2**: thiocyanate) into linear chains, resulting from the all-*trans* configuration, with the chains propagating along the crystallographic [111] direction (Fig. 1). The presence of Co1 in a general position and Co2 on an inversion center leads to a repeating [Co1···Co1···Co2] sequence along the chain. In compound **1**, the intrachain Co···Co separations amount to 5.7932(2) Å (Co1···Co1) and 5.7748(2) Å (Co1···Co2), whereas slightly shorter distances are observed for compound **2** (Co1···Co1: 5.5963(1) Å; Co1···Co2: 5.6113(1) Å).

Each chain is surrounded by six neighboring chains in a pseudo-hexagonal arrangement (Fig. S10). The equatorial bridging planes at the cobalt centers are coplanar, resulting in a sandwich-like packing motif in which layers of chains are separated by the axial pyridine ligands.

Despite their isostructural relationship, systematic differences in the interchain separations are observed between compounds **1** and **2**. Within the chain layers, the shortest chain–chain distance is 7.7031 Å for **1** and 8.3215 Å for **2**. In contrast, separations to chains in adjacent layers are 8.6406 and 8.8244 Å for **1**, and 8.3453 and 8.4356 Å for **2**. Notably, the trends are opposite for the two compounds, with the more pronounced differences occurring for chains arranged side by side within the layers.

These variations originate from subtle differences in the crystal packing. In compound **1**, short interchain Se···Se contacts (3.4902(5) and 3.5417(5) Å) are observed between neighboring chains, whereas in compound **2** the comparable interchain S···S distances (3.8926(8) and 3.9194(8) Å) are considerably longer (Fig. 2). These Se···Se separations approach the interchain contacts observed in trigonal gray selenium (≈3.44 Å),[27] while the S···S distances are somewhat larger than the intermolecular contacts observed in crystalline α-S_8 (≈3.80 Å).[28] Such distances fall within the range typically associated with weak secondary chalcogen–chalcogen interactions.[29] The presence of these contacts in **1** leads to a reduced lateral separation between adjacent chains within the layers, whereas the corresponding interactions in the sulfur analogue **2** are significantly weaker.

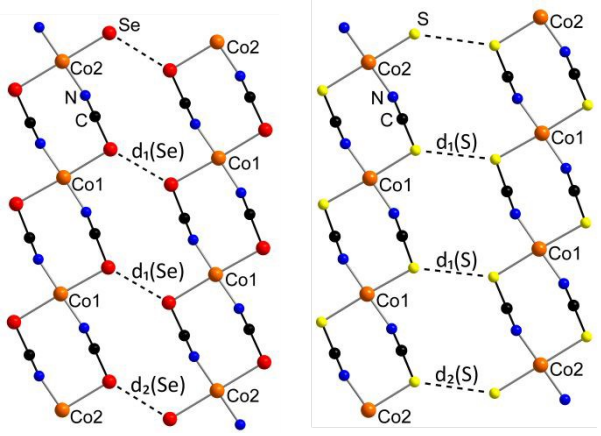

Fig. 2 Representation of the interchain interactions in compounds **1** (left) and **2** (right) between neighboring chains within the layer of chains in the crystal packing. Pertient distances: d_1(Se) 3.4902(5), d_2(Se) 3.5417(5), d_1(S) 3.8926(8), d_2(S) 3.9194(8) Å.

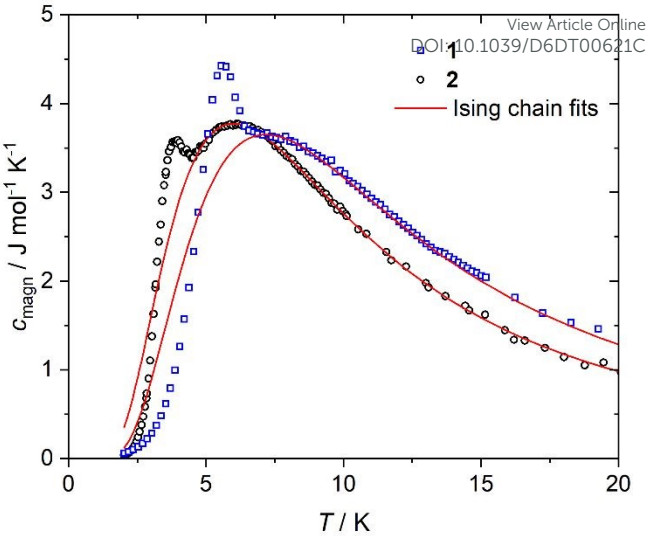

Fig. 3 Magnetic contribution to the molar heat capacity of compounds **1** (blue squares) and **2** (black circles). The corresponding fits using the Ising spin-chain model are shown as red lines.

The orientation of the axial pyridine ligands adjusts accordingly to accommodate the closer packing (Fig. S11). At the Co2 center, both pyridine rings are oriented nearly parallel to the chain direction (**1**: 165° and **2**: 168°). At the Co1 center, however, the two pyridine ligands adopt one nearly parallel orientation (**1**: 165° and **2**: 168°) and one approximately perpendicular orientation (**1**: 57° and **2**: 68°), with the pyridine ring in the selenium compound **1** showing the larger deviation from the ideal perpendicular arrangement.

In contrast, the separations between chains in adjacent layers are largely dictated by the length of the axial pyridine ligands coordinated to the cobalt centers and are therefore less sensitive to the nature of the bridging chalcogen atom.

Overall, compounds **1** and **2** represent closely related one-dimensional chain systems with long-range magnetic ordering, distinguished by subtle but systematic differences in both local coordination geometry and interchain contacts arising from the chalcogen substitution. Since interchain separations and specific interchain contacts directly affect the strength of interchain magnetic interactions and thus the magnetic order in such 1D chain compounds, thermodynamic investigations are required to quantify their impact. In this context, heat capacity measurements provide a sensitive probe to determine the magnetic ordering temperatures and to evaluate the effective intra- and interchain exchange interactions.

Heat capacity measurements

The temperature dependence of the heat capacity, c(T), provides a useful probe of magnetic interactions in low-dimensional systems and has previously been used to estimate intrachain interactions in related $[Co(NCS)_2L_2]_n$ chain compounds.[10] Fig. 3 shows the magnetic contribution to the molar heat capacity of compounds **1** and **2**, obtained by subtracting the fitted lattice contribution from the measured data (see Figs. S12 and S13 for details).

In both compounds, the magnetic molar heat capacity displays a broad maximum at approximately 5–6 K. This feature is consistent with short-range magnetic correlations in quasi-one-dimensional systems[6,11,30] and is further supported by the agreement with the Ising-chain model analysis, which reproduces both the position and shape of the anomaly. The high-temperature flank of this contribution was analyzed using the Ising spin-chain model with an effective spin S = ½ (see Supporting Information for details). This analysis yields effective exchange constants of J_{Ising} = 23.9 cm^{-1} for **1** and 20.3 cm^{-1} for **2**, indicating a stronger intrachain interaction in the selenocyanate compound. It should be noted that this estimate represents an approximation, as it neglects interchain interactions and assumes purely Ising-type exchange, which is not strictly valid for $[Co(NCS)_2L_2]_n$ chains. In related systems such as $[Co(NCS)_2(methoxypyridine)_2]_n$, deviations from the ideal Ising limit have been quantified using an XXZ model, yielding an exchange anisotropy ratio of J_{xx}/J_{zz} ≈ 0.21.[11] This indicates a strongly anisotropic, yet non-Ising, exchange regime. A more general approach, based on the Lines model employing ab initio-derived single-ion parameters within the POLY_ANISO framework, will therefore be used in the following sections to account for the anisotropic nature of the exchange interactions. Despite this deviation, the Ising model provides a useful effective description of the thermodynamic behavior in the relevant temperature range.

At lower temperatures, an additional sharp anomaly is observed in c(T), indicating the onset of long-range magnetic ordering. Such λ-type anomalies are typical for second-order phase transitions in quasi-one-dimensional magnetic systems, where weak interchain interactions drive the transition from short-range intrachain correlations to three-dimensional magnetic order. From the maxima of these anomalies, ordering temperatures of T_c = 5.8 K for **1** and 3.9 K for **2** were determined. The latter value is consistent with previous studies on the thiocyanate analogue **2**, where neutron diffraction experiments confirmed the onset of long-range ferromagnetic order below approximately 3.9 K.[13] These values agree within about 0.1 K with the transition temperatures obtained independently from THz-EPR spectroscopy (see section FD-FT THz-EPR measurements). The higher ordering temperature of **1** suggests stronger interchain magnetic interactions in the selenocyanate compound, consistent with the shorter Se···Se contacts between neighboring chains that reduce the lateral separation of the chains in the crystal structure. Importantly, while the intrachain energy scale is governed by single-ion anisotropy and intrachain exchange coupling, the magnetic ordering temperature is primarily determined by such interchain interactions, as evidenced by the structural differences between the two compounds (Figs. S10 and S11).

Interestingly, a slightly higher value of T_c = 4.25 K has previously been reported for compound **2** based on heat capacity measurements.[16] This discrepancy prompted us to examine the influence of sample preparation on the observed ordering temperature. Comparison of measurements on several batches revealed that mechanical treatment of the microcrystalline powders significantly affects the position of the anomaly. In particular, pressing the samples into pellets for calorimetric measurements leads to a noticeable increase of T_c. As shown in Fig. S13, a non-pressed sample of **2** exhibits a maximum in c(T) at T_c = 3.9 K, whereas pressing a sample from the same batch at 1000 bar—similar to the procedure employed in the recently reported measurement[16]—shifts this maximum to above 4.2 K. A comparable effect is observed for compound **1** (Fig. S12), where T_c = 5.8 K is obtained for the non-pressed sample, while slightly higher values of around 6.0 K have been reported previously.[16] These observations demonstrate that even moderate mechanical pressure, commonly applied during pellet preparation of powder samples, can influence the magnetic ordering temperature in such molecular chain magnets. This sensitivity is consistent with the structural characteristics discussed above, where relatively small variations in interchain separations and weak chalcogen–chalcogen contacts are expected to affect the interchain magnetic interactions responsible for stabilizing long-range magnetic order.

FD-FT THz-EPR measurements

Frequency-domain Fourier-transform (FD-FT) THz-EPR spectroscopy was employed to directly probe the magnetic excitations of compounds **1** and **2** and to experimentally assess changes in the magnetic anisotropy induced by the substitution of thiocyanate with selenocyanate as bridging unit. In contrast to thermodynamic methods, THz-EPR allows transition energies to be read out directly, without reliance on a specific model, and is therefore particularly suited for disentangling single-ion anisotropy and exchange-driven excitations in cobalt(II)-based chain compounds.

In such cobalt(II) compounds, two classes of magnetic excitations can be addressed in the THz frequency range. Single-ion transitions originate from the coupling of the S = 3/2 electron spin with the effective orbital angular momentum contribution associated with the partially unquenched orbital moment in octahedral cobalt(II) systems, resulting in three Kramers doublets (KDs) with predominant m_J = 1/2, 3/2, and 5/2. The lowest inter-KD transition (1/2 → 3/2) typically occurs in the range 100–300 cm^{-1}. In addition, low-energy excitations arise from magnetic exchange interactions along the chain and can be viewed as local spin reversals that effectively generate pairs of domain walls, which are typically observed between 5 and 30 cm^{-1}.[4] These excitations may further be influenced by interchain interactions below the magnetic ordering temperature.

To experimentally distinguish these magnetic excitations from field-independent contributions, the spectra were evaluated using magnetic-field division spectra (MDS), in which spectra recorded at a given field are divided by those measured at a field reduced by 1 T. This representation suppresses field-independent contributions and highlights magnetic transitions as positive or negative features. The corresponding low-frequency MDS are shown in Fig. 4 and reveal a single distinct field-dependent signal for both compounds.

This signal shifts to higher energies with increasing magnetic field and simultaneously broadens and decreases in intensity. From these data, zero-field transition energies of 23.6 cm^{-1} for **1** and 19.2 cm^{-1} for **2** were extracted (red dashed lines in Fig. 4). These energies are well below the calculated single-ion inter-KD transitions (vide infra) and fall within the energy range consistent with the experimentally and theoretically determined intrachain energy scales in such systems.[4,10] The observed transition is therefore assigned to the lowest intrachain excitation, Δ_{chain}, corresponding to the energy gap between the ground and the first excited state of the Ising spin chain, which depends on both the intrachain exchange interaction and the

View Article Online
DOI: 10.1039/D6DT00621C

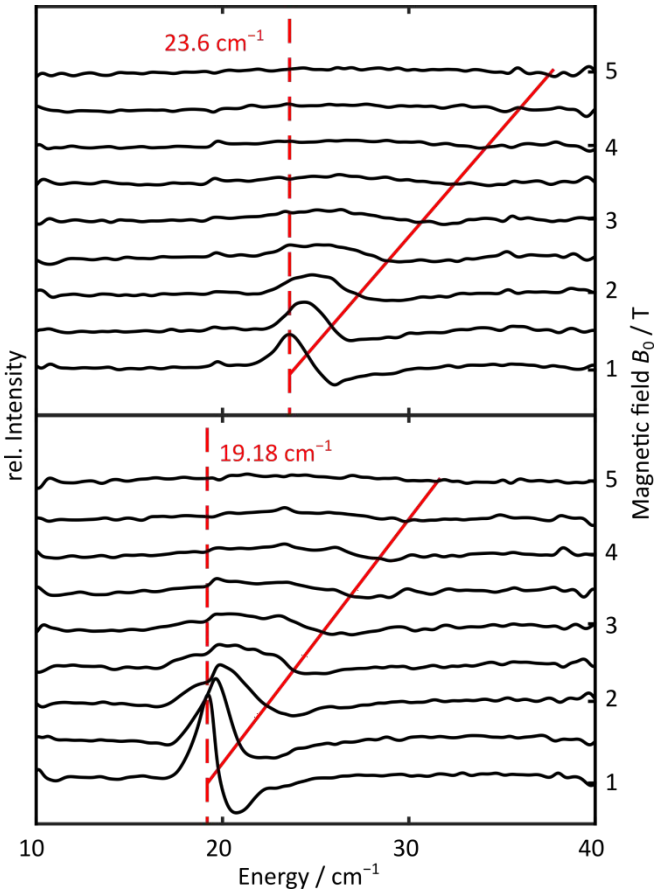

Fig. 4 FD-FT THz-EPR spectra of compounds 1 (top) and 2 (bottom) measured at 5 K. The black solid lines represent magnetic-field division spectra (MDS) obtained by dividing the raw spectrum recorded at B_0 by that measured at (B_0 – 1) T. The red dashed lines indicate the zero-field transition energy, while the red solid lines trace the field-dependent shift of this transition assuming fixed g_z values of 7.6 (1) and 6.7 (2).

single-ion anisotropy. Within the framework of anisotropic Ising-type spin chains, the excitation energy does not follow a simple analytical expression but reflects their combined energy scale set by these parameters, as discussed for related cobalt(II) systems.[6] Importantly, Δ_{chain} reflects the combined effect of intrachain exchange coupling and single-ion anisotropy and thus cannot be interpreted as a direct measure of the exchange interaction alone. From the field dependence of the chain excitation, effective g_z values of 7.6 for **1** and 6.7 for **2** were estimated. This trend is fully consistent with the ab initio results discussed below. Consequently, the low-frequency THz-EPR data already provide experimental evidence for both higher Δ_{chain} and larger g_z values in the selenocyanate compound **1**, reflecting its enhanced magnetic anisotropy compared to the thiocyanate analogue **2**.

The low-frequency spectra in Fig. 4 thus primarily probe intrachain magnetic excitations and are largely insensitive to weak interchain interactions. To access the latter and to identify the onset of long-range magnetic order, the temperature dependence of the chain excitation was investigated, as shown in Fig. 5.

The temperature-dependent MDS (Fig. 5) reveal a small but abrupt shift of the zero-field transition energy upon cooling, which marks the onset of three-dimensional magnetic ordering. From the magnitude of this shift, interchain coupling energies of Δ_{inter} =

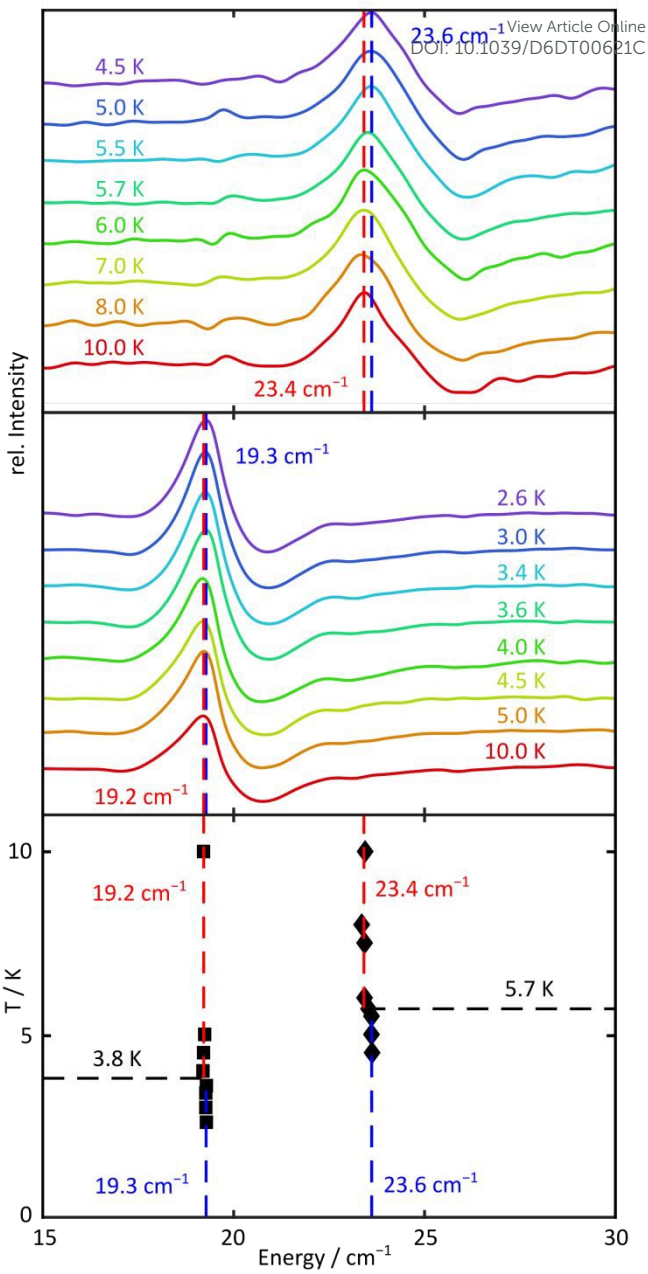

Fig. 5 Temperature dependence of the MDS (1 T/0 T) of compounds **1** (top) and **2** (middle), and extracted zero-field transition energies as a function of temperatures (bottom). Solid lines are color-coded from blue to red with rising temperature. The dashed vertical red and blue lines mark the average zero-field transition energies above (red) and below (blue) the respective ordering temperatures, while dashed horizontal black lines indicate the corresponding transition temperature.

0.2 cm^{-1} for **1** and 0.1 cm^{-1} for **2** were estimated. Notably, this shift is observed at temperatures of T_c = 5.7 K for **1** and 3.8 K for **2**, which is in good agreement with the values obtained from the heat capacity measurements. Although weak, the interchain interactions are consistently stronger in the selenocyanate compound. This trend correlates with the slightly shorter interchain Co···Co separations in **1** compared to **2**, as discussed in the structural section. This observation highlights that, while THz-EPR provides direct access to the intrachain excitation energy scale, the magnetic ordering

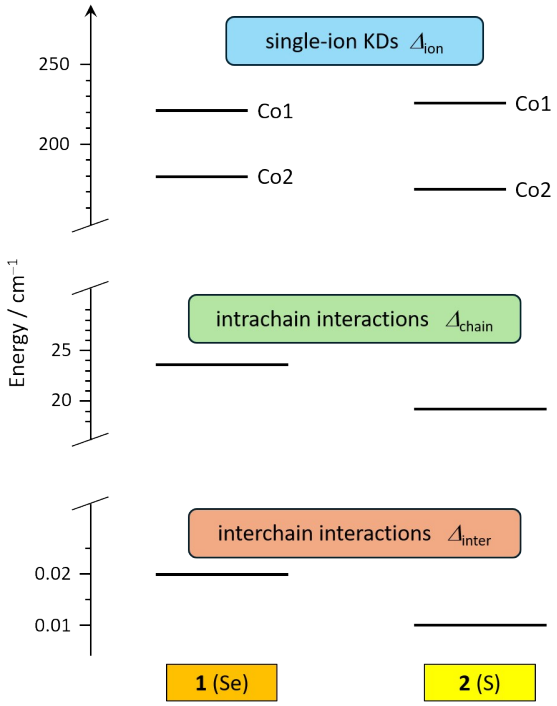

Fig. 6 Schematic energy-level diagram summarizing the hierarchy of magnetic excitations in compounds **1** and **2**. Single-ion inter-Kramers-doublet transitions (Δ_{ion}), intrachain excitations (Δ_{chain}), and interchain coupling energies (Δ_{inter}) are shown on their respective energy scales, illustrating the clear separation between local anisotropy-driven and collective exchange-driven magnetic phenomena.

temperature is governed by the comparatively weak interchain interactions.

Taken together, the low-frequency THz-EPR data demonstrate that the lowest-energy excitations in compounds **1** and **2** are governed by intrachain interactions, with interchain coupling contributing only weakly via a small temperature-dependent shift associated with the onset of long-range order. While these measurements provide direct access to Δ_{chain} and effective g_z values, they do not allow a microscopic determination of the underlying single-ion anisotropy parameters. To directly probe the zero-field splitting and resolve the individual Kramers doublets of the cobalt(II) centers, the analysis is therefore extended to the higher-frequency THz-EPR regime.

The hierarchy of magnetic excitations identified by THz-EPR spectroscopy and *ab initio* calculations is summarized schematically in Fig. 6, highlighting the distinct energy scales associated with single-ion anisotropy, intrachain interactions, and interchain coupling.

In addition to the low-energy chain excitations, numerous field-dependent features are observed at higher energies in both the MDS and magnetic-field subtraction spectra (Fig. S14). These signals originate from a combination of spin–phonon coupled modes and single-ion inter-KD transitions. Guided by ab initio calculations, the latter can be assigned to Δ_{ion}(Co2) = 179.5 cm^{-1} and Δ_{ion}(Co1) ≈ 220.8 cm^{-1} for **1**, and to Δ_{ion}(Co2) = 171.5 cm^{-1} and Δ_{ion}(Co1) = 225.5 cm^{-1} for **2**. Due to strong absorption in the vicinity of the Co1 transition in **1**, the corresponding transition energy can only be regarded as a rough estimate.

Interestingly, while the chain excitations and g_z values clearly increase from **2** to **1**, reflecting the enhanced anisotropy induced by the heavier chalcogen donor, the single-ion transitions do not follow a uniform trend. Whereas the Co2 center exhibits the expected increase in Δ_{ion} upon substitution of sulfur by selenium, the Co1 center shows the opposite behavior. This apparent discrepancy is accurately reproduced by the ab initio calculations and highlights the dominant influence of the orientation of the axial pyridine ligands on the single-ion anisotropy. As reported previously, the relative tilt of the pyridine ligands has a pronounced effect on the electronic structure of octahedral cobalt(II) centers.[4] In compounds **1** and **2**, the pyridine ligands at the Co2 center are nearly parallel to the chain direction with tilt angles of 15° and 12° for **1** and **2**, respectively (see Fig. S11), corresponding to a so-called parallel/parallel orientation.[4] For the Co1 center, one of the two pyridine ligands is also oriented parallel to the chain direction with similar tilt angles, whereas the second pyridine ligand exhibits a nearly perpendicular orientation with tilt angles of 57° in **1** and 68° in **2**, leading to an overall parallel/perpendicular orientation of the two pyridine rings at the Co1 center.

Consequently, for the Co1 center the change in ligand orientation outweighs the comparatively smaller effect of replacing thiocyanate by selenocyanate. These observations indicate that, for single-ion excitations, the axial ligand geometry plays a more prominent role than the chalcogen identity of the bridging ligand. Overall, compound **1** exhibits broader and less intense THz-EPR signals than **2**, which may partly be attributed to the increased molar mass and enhanced phonon density associated with the selenium-containing framework.

While THz-EPR spectroscopy provides direct experimental access to the relevant magnetic excitation energies and reveals clear and systematic differences between compounds **1** and **2**, it does not directly resolve the microscopic origin of the observed anisotropy effects at the level of individual coordination environments. In particular, the distinct trends observed for intrachain excitations and selected single-ion transitions indicate a subtle interplay between ligand identity and local coordination geometry. To rationalize these findings and to disentangle the respective contributions of chalcogen substitution and axial ligand orientation, ab initio calculations were performed based on the experimentally determined low-temperature crystal structures.

Computational studies

Theoretical investigations were performed to elucidate the single-ion magnetic properties of the octahedrally coordinated cobalt(II) centers in compounds **1** and **2** (see Computational Details). Ab initio CASSCF/CASPT2/RASSI-SO calculations were carried out using the model structures $[CoZn_2(NCX)_4(py)_2]^{2+}$ (X = Se for **1**, X = S for **2**) for all crystallographically independent cobalt(II) sites. The structural models (**1**-Co1, **1**-Co2, **2**-Co1, and **2**-Co2) were derived directly from the crystallographic data and are shown in Fig. S1.

For all cobalt(II) centers, a high-spin $^4T_{1g}[^4F]$ ground state was obtained, as expected for octahedrally coordinated cobalt(II) ions (Table S4). Upon inclusion of spin–orbit coupling, the $^4T_{1g}[^4F]$ term splits into six Kramers doublets (KDs), which span slightly larger energy ranges in **1** (**1**-Co1: 1580 cm^{-1}; **1**-Co2: 1502 cm^{-1}) than in **2** (**2**-Co1: 1439 cm^{-1}; **2**-Co2: 1407 cm^{-1}; Table S5). In all cases, the ground-state KD is well separated from the first excited KD (**1**-Co1: 224 cm^{-1};

View Article Online
DOI: 10.1039/D6DT00636C

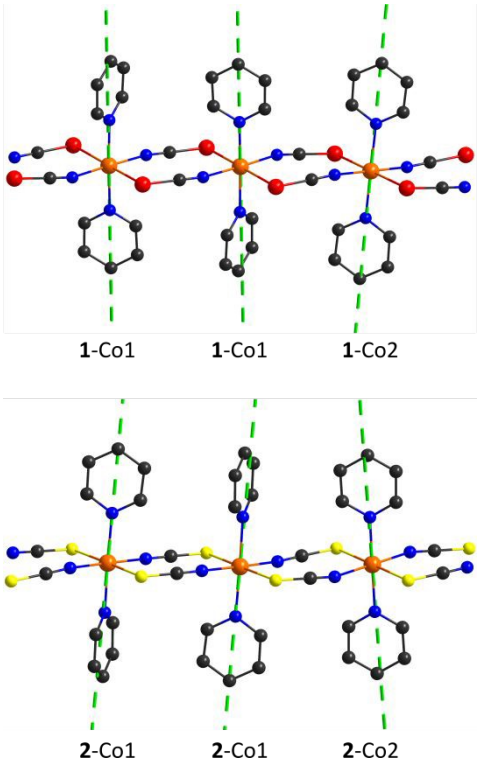

Fig. 7 Orientation of the magnetic easy axes of the ground-state Kramers doublets (S_{eff} = 1/2) for the crystallographically independent cobalt(II) centers in compound **1** (top) and compound **2** (bottom), projected onto the periodic chain structure. Hydrogen atoms have been omitted for clarity.

1-Co2: 177 cm^{-1}; **2**-Co1: 228 cm^{-1}; **2**-Co2: 174 cm^{-1}), justifying the use of an effective spin Hamiltonian with S_{eff} = 1/2 to describe the low-temperature magnetic properties.

The magnetic properties of the compounds are described using effective spin Hamiltonians adapted to the respective experimental and computational approaches. For the ab initio calculations, the electronic structure is treated explicitly, and the low-energy magnetic properties are mapped onto an effective S_{eff} = 1/2 description based on the ground-state Kramers doublet, yielding anisotropic *g* tensors. The analysis of the magnetic susceptibility data within the Lines model employs an anisotropic exchange Hamiltonian to describe the intrachain coupling between effective spin centers, while interchain interactions are treated within a mean-field approximation (*zJ'*).[4]

The Cartesian *g*-tensor components (S_{eff} = 1/2) for the lowest two KDs are summarized in Table S6. All cobalt(II) centers exhibit pronounced easy axis magnetic anisotropy ($g_z \gg g_{x,y}$) in the ground-state KD (Fig. S15), with the easy axes oriented nearly along the Co–N_{py} bond directions (Fig. 7), as expected for this class of compounds.[4] Notably, the orientation of the magnetic easy axis remains essentially unchanged upon chalcogen substitution and is approximately perpendicular to the chain direction, aligning with the axial pyridine ligands in both compounds. Thus, the observed differences in magnetic behavior originate predominantly from changes in the magnitude of the anisotropy rather than its orientation. The strongest magnetic anisotropy, as reflected by the g_z values, is found for **1**-Co1 (8.181), followed by **2**-Co1 (7.864), **1**-Co2 (7.587), and **2**-Co2 (6.483).

Previous studies have demonstrated that, in cobalt(II) compounds of the type $[Co(NCS)_2(L)_2]_n$ (L = pyridine derivatives), the magnitude of the single-ion anisotropy is governed by the relative orientation of the π-planes of the two axial pyridine ligands with respect to the chain direction, increasing in the order parallel/parallel < perpendicular/perpendicular < parallel/perpendicular.[4] This trend is fully consistent with the present results, where the Co2 sites adopt a parallel/parallel arrangement, while the Co1 sites exhibit a parallel/perpendicular geometry. Moreover, the $[N_4Se_2]$ donor environment in **1** leads to a systematic enhancement of the single-ion magnetic anisotropy compared to the $[N_4S_2]$ coordination in **2**, as reflected by larger g_z values for both Co1 and Co2 sites.

Due to symmetry operations along the chain, both compounds adopt a repeating [···Co1···Co1···Co2···]⍰ sequence, resulting in parallel alignment of the easy axes for neighboring Co1···Co1 pairs, while a small intersection angle is present between the easy axes of Co1 and Co2 sites (**1**: 13.6°; **2**: 14.9°, Fig. 7).

Following the established approach for cobalt(II)-based Ising chains, the experimental magnetic susceptibility data at low temperatures were analyzed within the Lines model, employing the single-ion parameters derived from the ab initio calculations to extract the intrachain exchange coupling.[4] Fits to the magnetic susceptibility data in the temperature range of 4.5–50 K were performed using the POLY_ANISO program employing finite *n*-membered spin rings, while all single-ion parameters were fixed to the ab initio values obtained above.

For sufficiently large ring sizes, this approach provides an excellent approximation to the infinite-chain limit, as demonstrated in previous studies, where convergence with respect to ring size has been systematically evaluated.[4,9,30] Weak ferromagnetic interchain interactions were taken into account by a mean-field correction (*zJ'* = 0.14 cm^{-1}) for both compounds. The analysis yielded comparable ferromagnetic intrachain exchange coupling constants (J_{Lines}) for compounds **1** and **2** (**1**: 3.24 cm^{-1}; **2**: 3.35 cm^{-1}; S_{eff} = 3/2; Fig. S16), indicating that chalcogen substitution has only a minor influence on the magnetic exchange interaction.

For comparison, effective Ising-type coupling constants, J_{calc}, were estimated from the energies of the highest-spin microstates of 12-membered spin rings, corresponding to an energy difference of 6 J_{calc} within this coupling scheme. The resulting values (**1**: 23.17 cm^{-1}; **2**: 20.71 cm^{-1}) are consistent with those obtained from the heat capacity analysis using the Ising model approximation.

Consequently, the higher intrachain excitation energy Δ_{chain} observed for compound **1** arises predominantly from its enhanced single-ion magnetic anisotropy rather than from a stronger exchange interaction. This conclusion is further supported by the simulated spin microstate distributions shown in Fig. S17, which reveal a more pronounced Ising-like character for compound **1**, in agreement with its larger g_z values and the smaller intersection angle between the local easy axes of magnetization at the Co1 and Co2 sites in the selenium compound **1** compared to the corresponding angle in the sulfur compound **2** (Fig. 7).

Overall, the computational results and the analysis of the magnetic susceptibility data consistently reproduce the characteristic energy scales associated with the single-ion and

intrachain magnetic excitations observed experimentally, which differ by roughly one order of magnitude (Fig. 5).

Conclusions

This study demonstrates that chalcogen substitution in otherwise closely related cobalt(II) chain compounds predominantly tunes the single-ion magnetic anisotropy rather than the intrachain exchange coupling. This conclusion is supported by a combined structural, thermodynamic, spectroscopic, and theoretical analysis of the isostructural chain compounds $[Co(NCX)_2(py)_2]_n$ (X = S, Se). The availability of high-quality low-temperature crystal structures for both compounds enabled a consistent correlation of structural, thermodynamic, spectroscopic, and theoretical results.

Heat capacity measurements provide direct access to the intrachain excitation energies of the ferromagnetic chains, which are found to be larger for the selenocyanate compound. THz-EPR spectroscopy further reveals significantly larger effective g_z values for the selenium derivative **1**, evidencing enhanced single-ion magnetic anisotropy. Analysis of the magnetic susceptibility data within the Lines model, in combination with *ab initio* calculations, shows that the intrachain exchange coupling constants (J_{Lines}) are very similar for both compounds. Consequently, the larger intrachain excitation energy observed for the selenocyanate compound originates predominantly from its enhanced single-ion magnetic anisotropy rather than from a stronger exchange interaction. The weak interchain interactions inferred from the temperature evolution of the THz-EPR spectra are consistent with the observed long-range ordering temperatures derived from heat capacity measurements and with the subtle differences in interchain separations derived from the crystal structures.

Ab initio CASSCF/CASPT2/RASSI-SO calculations reproduce the experimentally observed anisotropy trends and identify the softer donor character of selenium, in combination with the local coordination geometry effects, as the primary origin of the increased anisotropy in the selenocyanate compound. This effect is attributed to increased metal–ligand covalency and enhanced spin–orbit coupling contributions at the cobalt center. In particular, the smaller angle between the local easy axes at the crystallographically inequivalent cobalt(II) sites in compound **1** contributes to a more pronounced Ising-like character compared to the sulfur analogue.

Overall, this work demonstrates that chalcogen substitution in otherwise closely related cobalt(II) chain compounds predominantly tunes the magnetic anisotropy rather than the exchange interaction. The results highlight THz-EPR spectroscopy as a powerful and direct probe of magnetic excitations in low-dimensional magnetic systems and demonstrate how targeted ligand design provides a viable strategy to control magnetic anisotropy in ferromagnetic chain compounds.

Conflicts of interest

There are no conflicts to declare.

Data availability

Additional data supporting this article have been included in the supporting information: additional structural data, PXRD and IR spectra, heat capacity measurements, THz-EPR spectra, computational data, and fits using a spin-ring model. See DOI: 10.1039/b000000x/

CCDC-2523198 (**1**) and CCDC-2523199 (**2**) contain the supplementary crystallographic data for this paper.

Acknowledgements

This work was financially supported by the Deutsche Forschungsgemeinschaft (DFG, Project Nos. NA 720/5-2 and PL 155/16-2) and by the State of Schleswig-Holstein. We acknowledge the Helmholtz-Zentrum Berlin (HZB) for the allocation of synchrotron radiation beamtime at BESSY II (Project Nos. 231-11755 and 232-12507) and for financial support. We thank Dr. Tarek Al Said, Dr. Karsten Holldack, and Dirk Ponwitz for their technical support with the FD-FT THz-EPR measurements.

Notes and references

References

1 a) M. Atanasov, D. Aravena, E. Suturina, E. Bill, D. Maganas and F. Neese, *Coord. Chem. Rev.*, 2015, **289–290**, 177–214; b) R. Boča and C. Rajnák, *Coord. Chem. Rev.*, 2021, **430**, 213657; c) P. Kumar Sahu, R. Kharel, S. Shome, S. Goswami and S. Konar, *Coord. Chem. Rev.*, 2023, **475**, 214871; d) M. Wang, Z. Han, Y. Garcia and P. Cheng, *ChemPhysChem*, 2024, **25**, e202400396.

2 a) D. Li, L. Zheng, Y. Zhang, J. Huang, S. Gao and W. Tang, *Inorg. Chem.*, 2003, **42**, 6123–6129; b) Y. Oka, K. Inoue, H. Kumagai and M. Kurmoo, *Inorg. Chem.*, 2013, **52**, 2142–2149; c) T. d. A. Costa, M. Răducă, J. C. Rocha, M. A. Novak, R. A. A. Cassaro, M. Andruh and M. G. F. Vaz, *Inorg. Chem. Front.*, 2025, **12**, 1393–1402.

3 a) L. Bogani, A. Vindigni, R. Sessoli and D. Gatteschi, *J. Mater. Chem.*, 2008, **18**, 4750–4758; b) H.-L. Sun, Z.-M. Wang and S. Gao, *Coord. Chem. Rev.*, 2010, **254**, 1081–1100; c) R. Lescouëzec, L. M. Toma, J. Vaissermann, M. Verdaguer, F. S. Delgado, C. Ruiz-Pérez, F. Lloret and M. Julve, *Coord. Chem. Rev.*, 2005, **249**, 2691–2729.

4 M. Böhme and W. Plass, *Chem. Sci.*, 2019, **10**, 9189–9202.

5 J. Boeckmann and C. Näther, *Dalton Trans.*, 2010, **39**, 11019–11026.

6 M. Rams, M. Böhme, V. Kataev, Y. Krupskaya, B. Büchner, W. Plass, T. Neumann, Z. Tomkowicz and C. Näther, *Phys. Chem. Chem. Phys.*, 2017, 24534–24544.

7 a) F. A. Mautner, M. Traber, R. C. Fischer, A. Torvisco, K. Reichmann, S. Speed, R. Vicente and S. S. Massoud, *Polyhedron*, 2018, **154**, 436–442; b) Y. Wan, Y.-L. Zhang, Q. Zhang, S.-Y. Yang and D. Shao, *CrystEngComm*, 2024, **26**, 3771–3782; c) Y. Shen, M. Cui, H. Ohtsu, O. Stefanczyk, M. Yamashita and S.-I. Ohkoshi, *Chem. Eur. J.*, 2026, **32**, e03057.

8 a) Y. Zhang, Z.-Y. Liu, H.-M. Tang, B. Ding, Z.-Y. Liu, X.-G. Wang, X.-J. Zhao and E.-C. Yang, *Inorg. Chem. Front.*, 2022, **9**, 5039–5047; b) X.-B. Li, Y. Ma and E.-Q. Gao, *Inorg. Chem.*, 2018, **57**,

7446–7454; c) M. Wang, X. Gou, W. Shi and P. Cheng, *Chem. Commun.*, 2019, **55**, 11000–11012.

9 M. Böhme, A. Jochim, M. Rams, T. Lohmiller, S. Suckert, A. Schnegg, W. Plass and C. Näther, *Inorg. Chem.*, 2020, **59**, 5325–5338.

10 A. Jochim, T. Lohmiller, M. Rams, M. Böhme, M. Ceglarska, A. Schnegg, W. Plass and C. Näther, *Inorg. Chem.*, 2020, **59**, 8971–8982.

11 M. Rams, A. Jochim, M. Böhme, T. Lohmiller, M. Ceglarska, M. M. Rams, A. Schnegg, W. Plass and C. Näther, *Chem. Eur. J.*, 2020, **26**, 2837–2851.

12 a) Y.-Z. Zhang, B. S. Dolinar, S. Liu, A. J. Brown, X. Zhang, Z.-X. Wang and K. R. Dunbar, *Chem. Sci.*, 2018, **9**, 119–124; b) T. Charytanowicz, R. Jankowski, M. Zychowicz, S. Chorazy and B. Sieklucka, *Inorg. Chem. Front.*, 2022, **9**, 1152–1170.

13 S. Baran, A. Hoser, M. Rams, S. Ostrovsky, T. Neumann, C. Näther and Z. Tomkowicz, *J. Phys. Chem. Solids*, 2019, **130**, 290–297.

14 M. Ceglarska, M. Böhme, T. Neumann, W. Plass, C. Näther and M. Rams, *Phys. Chem. Chem. Phys.*, 2021, **23**, 10281–10289.

15 J. Boeckmann and C. Näther, *Chem. Commun.*, 2011, **47**, 7104–7106.

16 T. Neumann, M. Rams, Z. Tomkowicz, I. Jess and C. Näther, *Chem. Commun.*, 2019, **55**, 2652–2655.

17 a) S. Sottini, G. Poneti, S. Ciattini, N. Levesanos, E. Ferentinos, J. Krzystek, L. Sorace and P. Kyritsis, *Inorg. Chem.*, 2016, **55**, 9537–9548; b) J. M. Zadrozny, J. Telser and J. R. Long, *Polyhedron*, 2013, **64**, 209–217; c) E. A. Suturina, D. Maganas, E. Bill, M. Atanasov and F. Neese, *Inorg. Chem.*, 2015, **54**, 9948–9961; d) M. R. Saber and K. R. Dunbar, *Chem. Commun.*, 2014, **50**, 12266–12269; e) X.-N. Yao, M.-W. Yang, J. Xiong, J.-J. Liu, C. Gao, Y.-S. Meng, S.-D. Jiang, B.-W. Wang and S. Gao, *Inorg. Chem. Front.*, 2017, **4**, 701–705.

18 a) Y. Rechkemmer, F. D. Breitgoff, M. van der Meer, M. Atanasov, M. Hakl, M. Orlita, P. Neugebauer, F. Neese, B. Sarkar and J. van Slageren, *Nat. Commun.*, 2016, **7**, 10467; b) M. Böhme, S. Ziegenbalg, A. Aliabadi, A. Schnegg, H. Görls and W. Plass, *Dalton Trans.*, 2018, **47**, 10861–10873; c) M. H. Pohle, M. Böhme, T. Lohmiller, S. Ziegenbalg, L. Blechschmidt, H. Görls, A. Schnegg and W. Plass, *Chem. Eur. J.*, 2023, **29**, e202202966; d) M. H. Pohle, T. Lohmiller, M. Böhme, M. Rams, S. Ziegenbalg, H. Görls, A. Schnegg and W. Plass, *Chem. Eur. J.*, 2024, **30**, e202401545.

19 G. M. Sheldrick, *Acta Crystallogr. A*, 2015, **71**, 3–8.

20 G. M. Sheldrick, *Acta Crystallogr. C*, 2015, **71**, 3–8.

21 a) J. Nehrkorn, K. Holldack, R. Bittl and A. Schnegg, *J. Magn. Reson.*, 2017, **280**, 10–19; b) A. Schnegg, J. Behrends, K. Lips, R. Bittl and K. Holldack, *Phys. Chem. Chem. Phys.*, 2009, **11**, 6820–6825.

22 a) C. van Alsenoy, *J. Comput. Chem.*, 1988, **9**, 620–626; b) J. L. Whitten, *J. Chem. Phys.*, 1973, **58**, 4496–4501; c) E. J. Baerends, D. E. Ellis and P. Ros, *Chem. Phys.*, 1973, **2**, 41–51.

23 J. P. Perdew, *Phys. Rev. B*, 1986, **33**, 8822–8824.

24 F. Weigend and R. Ahlrichs, *Phys. Chem. Chem. Phys.*, 2005, **7**, 3297–3305.

25 a) S. G. Balasubramani, G. P. Chen, S. Coriani, M. Diedenhofen, M. S. Frank, Y. J. Franzke, F. Furche, R. Grotjahn, M. E. Harding, C. Hättig, A. Hellweg, B. Helmich-Paris, C. Holzer, U. Huniar, M. Kaupp, A. Marefat Khah, S. Karbalaei Khani, T. Müller, F. Mack, B. D. Nguyen, S. M. Parker, E. Perlt, D. Rappoport, K. Reiter, S. Roy, M. Rückert, G. Schmitz, M. Sierka, E. Tapavicza, D. P. Tew, C. van Wüllen, V. K. Voora, F. Weigend, A. Wodyński and J. M. Yu, *J. Chem. Phys.*, 2020, **152**, 184107; b) *TURBOMOLE V7.6 2022, a development of University of Karlsruhe and Forschungszentrum Karlsruhe GmbH, 1989-2007, TURBOMOLE GmbH, since 2007; available from http://www.turbomole.org*.

26 a) L. F. Chibotaru, L. Ungur, C. Aronica, H. Elmoll, G. Pilet and D. Luneau, *J. Am. Chem. Soc.*, 2008, **130**, 12445–12455; b) L. Ungur, W. van den Heuvel and L. F. Chibotaru, *New J. Chem.*, 2009, **33**, 1224.

27 P. Cherin and P. Unger, *Inorg. Chem.*, 1967, **6**, 1589–1591.

28 S. J. Rettig and J. Trotter, *Acta Crystallogr. C*, 1987, **43**, 2260–2262.

29 R. Gleiter, G. Haberhauer, D. B. Werz, F. Rominger and C. Bleiholder, *Chem. Rev.*, 2018, **118**, 2010–2041.

30 M. Rams, T. Lohmiller, M. Böhme, A. Jochim, M. Foltyn, A. Schnegg, W. Plass and C. Näther, *Inorg. Chem.*, 2023, **62**, 10420–10430.

View Article Online
DOI: 10.1039/D6DT00621C

Data availability

Additional data supporting this article have been included in the supporting information: additional structural data, PXRD and IR spectra, heat capacity measurements, THz-EPR spectra, computational data, and fits using a spin-ring model. See DOI: 10.1039/b000000x/ CCDC-2523198 (**1**) and CCDC-2523199 (**2**) contain the supplementary crystallographic data for this paper.